Compositionally flexible alloy design towards recycling mixed stainless steel scraps

Liu, Qiqi; Wang, Lingyu; Wang, Chenchong; Wu, Yuxiang; Zhang, Zhen; Wei, Xiaolu; Li, Yong; van der Zwaag, Sybrand; Xu, Wei; More Authors

DOI
10.1016/j.jmst.2024.11.041

Publication date
2025

Document Version
Final published version

Published in
Journal of Materials Science and Technology

Citation (APA)
Liu, Q., Wang, L., Wang, C., Wu, Y., Zhang, Z., Wei, X., Li, Y., van der Zwaag, S., Xu, W., & More Authors (2025). Compositionally flexible alloy design towards recycling mixed stainless steel scraps. *Journal of Materials Science and Technology*, *225*, 227-239. https://doi.org/10.1016/j.jmst.2024.11.041

Journal of Materials Science & Technology 225 (2025) 227–239

Contents lists available at ScienceDirect

Journal of Materials Science & Technology

journal homepage: www.elsevier.com/locate/jmst

Research Article

Compositionally flexible alloy design towards recycling mixed stainless steel scraps

Qiqi Liu[a,1], Lingyu Wang[a,1,*], Chenchong Wang[a], Yuxiang Wu[b], Zhen Zhang[c], Xiaolu Wei[a], Yong Li[a], Jiahua Yuan[a], Jun Hu[a], Dengping Ji[d], Sybrand van der Zwaag[e], Yizhuang Li[a], Wei Xu[a,*]

[a] State Key Laboratory of Rolling and Automation, Northeastern University, Shenyang 110819, China
[b] Department of Materials Science and Engineering, Monash Unversity, Clayton, Victoria 3800, Australia
[c] Center for Advanced Laser Technology, Hebei University of Technology, Tianjin 300401, China
[d] Zhejiang Tsingshan Iron & Steel Co., Ltd., Lishui 323903, China
[e] Novel Aerospace Materials Group, Faculty of Aerospace Engineering, Delft University of Technology, 2629 HS, Delft, The Netherlands

ARTICLE INFO

Article history:
Received 15 July 2024
Revised 28 October 2024
Accepted 11 November 2024
Available online 21 December 2024

Keywords:
Compositionally flexible alloys
Austenitic stainless steels
Scrap recycling
Recycling-oriented alloy design

ABSTRACT

Recycling-oriented alloy design is a crucial part of material sustainability, as it reduces the need for raw material extraction and minimises environmental impact. This requires that scraps be reused or repurposed effectively, even when the scraps are co-mingled and have higher costs for further sorting and separation. In this work, we explore an alloy design concept by creating a compositionally flexible domain that can recycle multiple alloy grades and yet maintain relatively consistent properties across chemical variations. This is demonstrated through the Fe-Cr-Ni-Mn system to identify compositionally flexible austenitic stainless steels (CF-ASS) and accommodate the recycling of mixed austenitic stainless steel scraps. Alloys within the nominal composition spaces exhibit relatively consistent mechanical properties and corrosion resistance despite significant variations in different alloy compositions. We illustrate how we can utilise the compositionally flexible austenitic stainless steels to recycle mixed 200 and 300-series stainless steel and ferronickel scraps, demonstrating its practical viability. While this demonstration focuses on the stainless steel system, the underlying principles can be extended to other systems related to mixed scrap recycling.

1. Introduction

The steel industry contributes approximately 25 % to global industrial carbon emissions and around 11 % to total global CO_2 emissions [1,2]. Mitigating greenhouse gas emissions in the steel sector is critical for achieving the climate targets outlined in the Paris Agreement. It is acknowledged that a substantial portion of carbon emissions can be reduced by adopting clean energy and reductants during mineral extraction and ore reduction [3]. For example, the use of hydrogen to produce direct reduced iron from iron ore regains significant interest in steel metallurgy [4–6]. In parallel to the decarbonisation of raw material extraction, recycling and reintegrating used materials and scraps back into the production chain is equally important for achieving carbon neutrality in the steel lifecycle [7].

The core technical challenge regarding metal recycling originates from the current diverse alloy families used in engineering systems, as intricate alloying strategies are required for performance enhancement. In some cases, this renders the complete separation of alloying elements back to each elemental recycling stream nearly impossible [8–11]. We can summarise several strategies related to alloy development in metal recycling, which revolve around the chemistry of alloys and address various aspects of complex metal recycling problems [12,13]. First, it is desirable that one could engineer microstructures of selected compositions to create alloy variants satisfying multiple property requirements in one engineering system. This effectively bypasses the complexity of multiple alloy chemistries and related costs for separation in recycling. This has stimulated increasing discussions on "uni-alloys" or "cross-over alloys" (i.e., one composition for multiple applications). In automotive applications, recent developments such as “UniSteel” [14] and “UniCast” [15] alloys aimed to reduce the number of steels

* Corresponding authors.
E-mail addresses: wanglingyu@ral.neu.edu.cn (L. Wang), xuwei@ral.neu.edu.cn (W. Xu).
[1] These authors contributed equally to this work.

https://doi.org/10.1016/j.jmst.2024.11.041
1005-0302/

and aluminium alloys used in car body-in-white (BIW) structures. By employing a single material, the resulting BIW can be easily recycled and remelted with less or even without extensive sorting and classification. While the “uni-alloys” may have a single composition, the heat treatments can be tailored to generate similar microstructures comparable to commercial grades (e.g. intercritical annealing for dual phase steels, quenching and partitioning for Q&P steels, and full austenization for press hardened steels) [14]. Based on similar principles, the “cross-over alloys” are recently developed in wrought aluminium alloys [16]. They are designed to inherit the advantages of both highly formable (i.e., 3xxx/5xxx series) and precipitation hardenable (i.e., 2xxx/7xxx series) aluminium alloys, effectively overcoming the traditional trade-off between strength and formability. The concept of "uni-alloys" envisions a long-term plan that integrates substantial co-developments in engineering systems and alloys. It aims to achieve minimal chemical diversity within a single engineering system, benefiting from advancements in processing and microstructure engineering to extend the property Pareto fronts with a limited variety of alloying elements. In the meantime, its large-scale applications can only be incentivised based on acceptable costs when the end-of-life cycle is taken into account.

We are currently in a transition period, moving from existing scrap utilisation practices to system designs where recycling mindset is fully integrated at the design stage. The sorting and separation processes represent significant overheads in recycling, and effective utilisation of scrap is a key emphasis. To increase the use of scrap and minimise the reliance on more primary metals for diluting impurities, there is a focused emphasis on developing alloy variants or processing methods that are more tolerant of impurities (e.g. Cu in steels [17–19] and Fe in aluminium alloys [20]). Such impurity effects in recycling are usually considered at a relatively small amount, and these impurity elements are either removed, diluted, or accommodated.

There are important scenarios where scraps are mixed at a concentrated level and even across multiple alloy systems, which require certain flexibilities in recycling alloy chemistry. This is particularly relevant when various streams of alloy scraps are commingled, and the costs and carbon emissions associated with separating these scraps exceed those required for direct remelting. This catalyses an alternative approach to designing recycling-oriented alloys, which involves employing compositionally flexible alloys (CFA). This concept aims to deliver essential properties within a composition range rather than adhering strictly to specific compositions [21]. The initial demonstration related it to face-centred cubic (FCC) high entropy alloys (HEAs), where mixed stainless steel and nickel superalloy scraps (up to 17 different elements) can be utilised to create HEAs with consistent yield strength. CFAs are likely to become increasingly relevant with the emergence of more highly alloyed materials in the market, e.g., with the potential adoption of HEAs [22,23]. There are several additional practical considerations for the implementation of CFAs: (1) We do need to consider the available elemental pools for the phase stability of the microstructure template. For example, in single-phase FCC-based compositionally flexible alloys, a high content of alloying elements such as Co and Ni is usually needed to stabilize the FCC phase. Existing alloy scraps may not always be recycled together; for instance, while stainless steels are prevalent in multiple applications (construction, transportation, chemical industry, kitchen appliances, etc.), Ni- and Co-based superalloys are predominantly utilised in the aerospace industry. (2) Designation of "nominal composition space": the absence of a standardized "nominal composition space" for designed CFAs may further impede their commercialisation, as most manufacturers are accustomed to producing well-classified materials with some tolerances on chemistry variations. Establishing clearly identified composition spaces with stable property outputs could provide the necessary guidelines to encourage manufacturers to transition towards a more circular and flexible alloy production process.

Differing from high-entropy alloys, stainless steel ranks as the third most utilized material following carbon steel and aluminium [24,25]. Since stainless steels typically have high alloying additions, the recycling of end-of-life (EOL) scrap stainless steels becomes particularly promising. Judging by chromium and nickel contents, stainless steel can generally be categorized into ferritic stainless steel (Fe-Cr based 400 series) and austenitic stainless steel (Fe-Cr-Ni based 300 series) [25,26]. Due to limitations in recycling technology, the recycling rates of various categories of EOL stainless steel vary. At present, the recycling process for waste steel primarily involves collection, cleaning, shredding, and separation [9]. During the separation process, scrap ferritic stainless steels possessing ferromagnetic properties often remain undetected and become intermixed with carbon steel scrap. Consequently, 29 % of EOL stainless steels (mainly ferritic stainless steels) are downgraded to carbon steel for recycling [24], resulting in the Cr within being treated as an impurity element. This necessitates additional primary steel for dilution during recycling, leading to chromium resource loss [27]. In contrast, non-magnetic austenitic stainless steel scrap can be separated from mixed scrap by magnetic separators with recovery rates as high as 70 % [25]. However, the high cost of Ni in 300 series stainless steels has triggered the replacement of Ni by Mn in the last few decades, leading to the development of Fe-Cr-Ni-Mn based 200 series stainless steels [28,29]. Since both 200 and 300 series stainless steels are paramagnetic, the separation of mixed 200 and 300 series scrap is difficult and requires costly setups [30]. Direct remelting of mixed stainless steels scrap can be an alternative solution besides scrap sorting.

In this contribution, we apply the CFA concept to design low cost, compositionally flexible austenitic stainless steels that are well-suited for recycling. The alloying additions may come from 200 series and 300 series stainless steels which are already recycled extensively [31,32], while other steel grades such as duplex stainless steels or high manganese steels may also be integrated into the cycle. Although impurity elements such as C, N, and Mo are inevitably introduced during industrial mixing and remelting, all alloy designs considered in this study are based on the Fe-Cr-Ni-Mn quaternary system, with the effects of impurities and the treatments to be explored in future investigations. The introduction of large amounts of the C element may reduce the corrosion resistance, then the removal of the impurity element C at the remelting stage is a more appropriate decision [33]. In the following sections, screening criteria for such compositionally flexible austenitic stainless steels (CF-ASS) are proposed and two nominal composition spaces are discovered to produce CF-ASS with mechanical and corrosion properties comparable to commercial austenitic stainless steels as well as high compositional flexibilities. Furthermore, it is demonstrated that these composition spaces can be readily achieved through the use of mixed 200 and 300 series scraps, facilitated by ferronickel master alloys. This research establishes a framework that can be extended to other metal classes and their respective research communities, providing guidance for revising existing pools of commercial alloys and developing roadmaps for the transition to recycling-oriented alloy design.

2. Construction of the CF-ASS nominal composition space

The scope of this work includes two main parts. The first part is to construct a preliminary composition space (PCS) that is suitable to produce austenitic stainless steel using commercially available stainless steel. To achieve this, screening criteria based on phase stability, minimum Cr content, and source availability are established, and the screening results are presented (Section 2.1).

The second part is to identify the nominal composition space for the designed CF-ASS by setting property variation thresholds for compositions within the PCS. These two steps will ensure the designed CF-ASS to have maximized variability in chemistry but stable property output. Accordingly, property predictors are constructed (Section 2.2) so that the search for the composition subdomain is guided by specified property restrictions (Section 2.3). Fig. 1 shows a schematic diagram of each screening process and associated potential candidate alloy numbers. The following sections detail the screening criteria, property prediction results, and the search for composition spaces.

2.1. Preliminary composition space screening

2.1.1. Composition screening based on phase stability

Two phase stability criteria can be identified for austenitic stainless steels: it must remain fully austenitic at elevated temperatures, and it should not undergo martensitic transformations upon quenching. To meet the first requirement, the candidate alloys in this study are required to maintain >99 vol.% austenite above 800 °C (1073 K). Equilibrium calculations are performed using Thermo-Calc and the TCFE9 database. The second criterion involves determining the martensite start temperature (M_s). Estimating M_s within the current alloying composition range requires a predictive model with high extensibility and accuracy. Existing empirical equations and thermodynamic models exhibit limited generalizability when applied to multiple alloy systems, particularly when the composition range to be predicted extends beyond the calibrated space used to develop the models. Here, we used a deep-learning model (DDM-CNN model) that integrates thermodynamic calculations, deep data mining (DDM), and convolutional neural network (CNN) techniques [34]. The approach combines thermodynamic calculations and deep AI to model the M_s using a deep data mining (DDM)-embedded deep learning (DL) approach. Firstly, DDM was used to establish a hierarchical database with three levels of information: alloy compositions, thermodynamic data derived from these compositions (including SFE and chemical driving forces for phase transformations), and frictional work acquired through machine learning. Then, the hierarchical database from DDM is embedded in a CNN to obtain the M_s prediction results. Compared to traditional models, this approach combines the advantages of thermodynamics, traditional machine learning, and deep learning models, which breaks through the limitations related to composition space, and enhances the extensibility. As demonstrated in our previous work [34], its primary advantage over other existing models lies in its ability to provide reasonable predictions (with a mean average error of ± 25 K) for the M_s temperature across a wide composition range (e.g., Mn content up to 30 wt.% and Cr content up to 20 wt.%). Therefore, the high extensibility of the DDM-CNN model can help find relatively accurate M_s for candidate compositions. Considering the prediction error associated with the DDM-CNN model, a limit of 350 K was set for the M_s temperature, and compositions exceeding this threshold were eliminated.

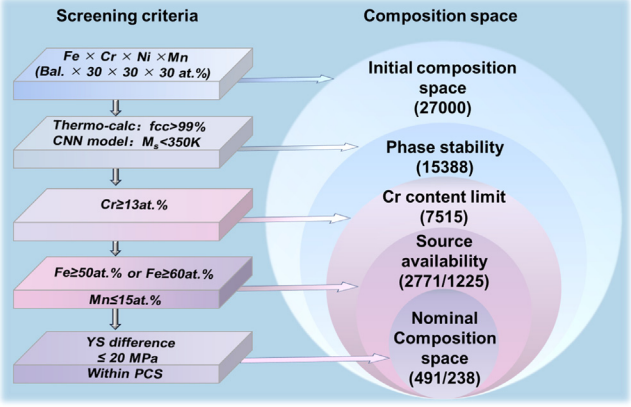

Fig. 1. A schematic diagram showing the alloy design process, the number below the text represents the number of candidate compositions after each screening process.

2.1.2. Composition screening based on Cr content

A critical performance metric for austenitic stainless steels is their corrosion resistance. In the current work, a simple rule-of-thumb principle for stainless steel was applied, mandating a minimum Cr content of 13 at.% for the alloys that pass the phase stability screening. This threshold was established based on the common understanding that steels with lower Cr content are typically not considered "stainless" [35]. Further calculations pertaining to corrosion-related properties, such as pitting potentials, were not conducted here. This decision was influenced by an examination of available predictive models, which revealed unsatisfactory performance metrics (predictive R^2 < 0.8), including those based on machine learning approaches [36]. The inaccuracies observed can be attributed primarily to the significant variations in testing conditions reported in the literature and the absence of high-quality databases.

2.1.3. Composition screening based on source availability

The criterion for the availability of scrap stainless steel sources is an important consideration. The objective of this study is to engineer compositionally flexible austenitic stainless steels that can accommodate mixed sources of stainless steel scraps. Here, the compositions of commonly used 200 and 300-series stainless steels are provided in Supplementary Information (see Table S1) and are the focus of this work. Among commercial stainless steel grades, Mn is relatively uncommon, as high Mn (stainless) steels are less frequently used. Consequently, an upper limit of 15 at.% Mn was imposed. No specific limits were imposed for Cr and Ni contents, given their prevalence in stainless steels designed for critical service environments. The retained Fe content was, in initial approximation, regulated within the range of 50 %–80 % (atomic fraction), aligning with the composition of most commercial products. However, considering alloy costs, a minimum Fe content exceeding 60 at.% was also explored in subsequent alloy designs.

2.1.4. Preliminary composition space after screening

Fig. 2 shows the composition space following each stage of screening. The screening starts with a 30 × 30 × 30 cubic gride containing 30^3 (27,000) candidate compositions (step size of 1 at.%). Among the total of 27,000 candidate compositions, 17,806 satisfy the first phase stability criterion, exhibiting >99 vol.% FCC at 800 °C (Fig. 2(a)). It is notable that most of the remaining candidate compositions have high Mn and Ni contents as they are strong austenite stabilizers. For the second phase stability criterion, compositions with low alloy concentrations are further eliminated due to the fact that the addition of Cr, Ni, and Mn decreases the M_s temperature. This refinement process results in 15,388 candidate compositions being retained (Fig. 2(b)). Finally, the requirement for the Cr, Mn, and Fe contents further cut the composition space to contain 2898 candidate compositions (Fig. 2(c)), which constitute the preliminary composition space to be investigated in subsequent sections.

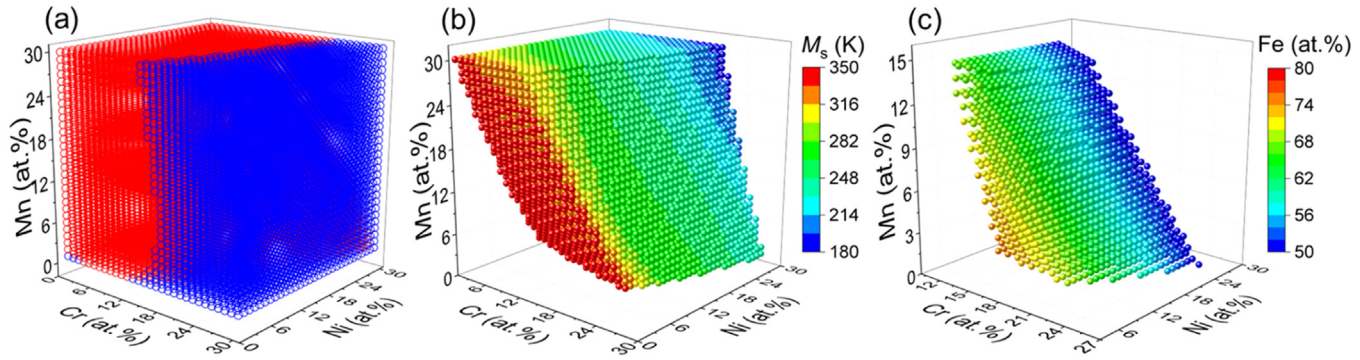

Fig. 2. Construction of the composition space. (a) Alloys satisfied the FCC criterion are marked with red circles and the ones that failed are marked with blue circles. (b) Alloys with the M_s temperature lower than 350 K. (c) Alloys with Cr content greater than 13 at.%, Mn content <15 at.%, and Fe content between 50 at.% to 80 at.%.

2.2. Property prediction

2.2.1. Strength prediction

Solid solution strengthening is the main factor contributing to the variation in yield strength of Fe-Cr-Ni-Mn alloys. The contribution of solid solution strengthening to yield strength was calculated using the simplified elastic model proposed by Varvenne et al. [37]. The simplified elastic distortion version of the model consists of the Peierls stress at 0 K ($\tau_{y,0}$) and the energy barrier ΔE_b that needs to be overcome to move dislocations (Eqs. (1) and (2)).

$$\tau_{y,0} = 0.01785\alpha^{-\frac{1}{3}}\bar{\mu}\left(\frac{1+\bar{\nu}}{1-\bar{\nu}}\right)^{\frac{4}{3}}\left[\frac{\sum_n c_n \Delta V_n^2}{b^6}\right]^{\frac{2}{3}} \quad (1)$$

$$\Delta E_b = 1.5618\alpha^{\frac{1}{3}}\bar{\mu}b^3\left(\frac{1+\bar{\nu}}{1-\bar{\nu}}\right)^{\frac{2}{3}}\left[\frac{\sum_n c_n \Delta V_n^2}{b^6}\right]^{\frac{1}{3}} \quad (2)$$

where $\alpha = 0.123$, is the line tension parameter, b is the mean Burger's vector, c_n is the concentration of the element n and ΔV_n is the misfit volume. The model requires $\bar{\mu}$ and $\bar{\nu}$ values at the specified composition and temperature T. A rule-of-mixtures average of $\bar{\mu}$ and $\bar{\nu}$ was employed without measuring the elastic constants of the predicted alloys. At a given temperature T and strain rate, ε, the standard thermal activation theory leads to the critical solution of the shear stress:

$$\tau\left(T,\varepsilon\right) = \tau_{y,0}(T)\left[1-\left(\frac{kT}{\Delta E_b(T)}\ln\frac{\varepsilon_0}{\varepsilon}\right)^{\frac{2}{3}}\right] \quad (3)$$

k is Boltzmann's constant, ε_0 is the reference strain rate (set as 10^4 s^{-1}) [37], ε was set to 10^{-3} s^{-1} and T was set at 300 K. The calculated yield strength depends substantially on ΔV_n (the volumetric misfit of each atom) calculated as the difference between the volume of the nth atom (V_n) and the atomic volume of the alloy ($\bar{V} = \sum_n c_n V_n$). The values of V_n used in this work can be found in Table S2. The shear stress shown in the above equations can be converted to tensile stress using the Taylor factor ($\sigma = M\tau$, M=3.06 [38]).

The contribution to strengthening calculated in Eq. (3) accounts only for the alloying element effect on solid solution strengthening, while additional strengthening mechanisms may be present in experimentally smelted alloys. To incorporate strengthening from grain refinement, an averaged Hall-Petch parameter of 400 MPa·μm$^{-0.5}$ was employed. This typically leads to an increase of ~60 ± 13 MPa in yield strength for samples with an average grain size of 50 ± 20 μm, which is typical for our samples subjected to cold rolling and subsequent annealing. Additionally, the samples typically contain 0.3 ± 0.1 at.% of C and N so an additional contribution of 22 ± 10 MPa was added to account for interstitial strengthening (using a strengthening factor of 75 MPa per at.%) [39].

2.2.2. Deformation mode estimation by stacking fault energy

Austenitic stainless steels can have dynamically evolving microstructures and deformation mechanisms under plastic deformation. The plastic behaviour of austenitic steels is determined by their deformation mechanisms and strain hardening. Importantly, the presence of different plasticity-driven transformation products can modify the magnetic properties of deformed stainless steels, particularly if ferromagnetic martensite forms. For practical scenarios such as maritime applications, it is essential for the designed CF-ASS to maintain consistent magnetic properties, i.e., remaining paramagnetic, both before and after deformation. The deformation mode of austenite is strongly dependent on the stacking fault energy (SFE), which is predominately composition-dependent. The SFE of austenite was calculated using the classical Olson-Cohen thermodynamic model [40]:

$$\gamma_{SFE} = 2\rho\Delta G^{\gamma\to\varepsilon} + 2\sigma^{\gamma/\varepsilon} \quad (4)$$

where ρ represents molar surface density of atoms in the {111} planes, $\sigma^{\gamma/\varepsilon}$ is the interfacial energy of the γ/ε interfaces and $\Delta G^{\gamma\to\varepsilon}$ is the molar Gibbs energy change from the FCC to the hexagonal close-packed (HCP) structure. Detailed calculations can be found in the Supplementary Information. In the current study, we encompass a wide range of composition distribution; it is noteworthy that most of these equations originate from studies of medium Mn steels [41], potentially resulting in deviation in prediction outcomes for low Mn, high Cr, and Ni cases. We consider that the predicted SFE values would offer qualitative guidance regarding the potential deformation mechanisms of the alloys. Further elaboration on this matter will be provided in subsequent sections.

2.2.3. Property prediction results

According to the calculation results shown in Fig. 3(a), the predicted YS range of the PCS is between 130 MPa and 230 MPa, with the majority of candidate compositions having YS greater than 150 MPa. It is important to note that these prediction results only account for basic strengthening mechanisms, suggesting that the final product should be able to achieve higher mechanical properties when subjected to additional thermomechanical processing. For the SFE prediction shown in Fig. 3(b), it is seen that while a small fraction of candidate alloys show low SFE (~15–20 mJ/m^2) that may lead to the transformation-induced plasticity (TRIP) effect, most of the candidate alloys are predicted to have relatively high SFE (> 36 mJ/m^2), indicating deformation twinning and dislocation slip will be the dominate deformation mechanisms for the majority of candidate compositions in the PCS and the ferromagnetic phase will not appear during deformation.

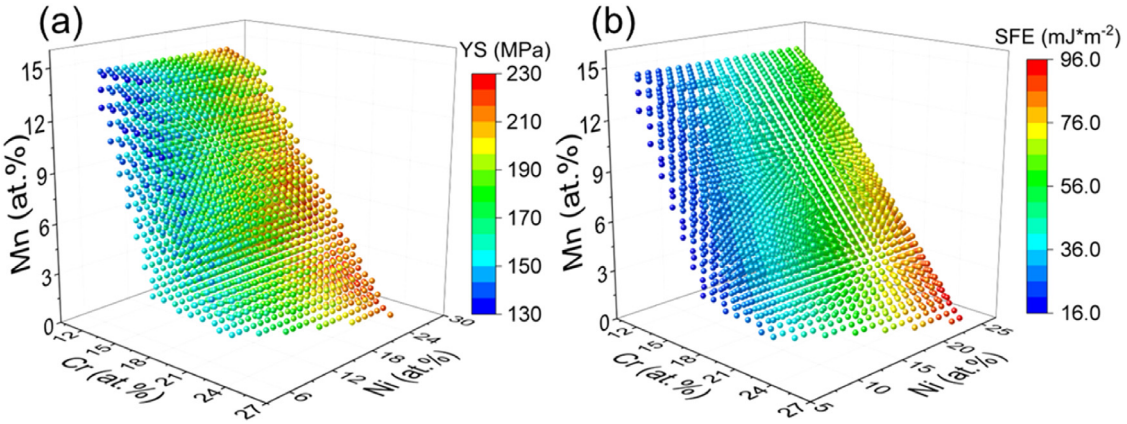

Fig. 3. (a) Predicted yield strength and (b) SFE for the alloys within the composition space.

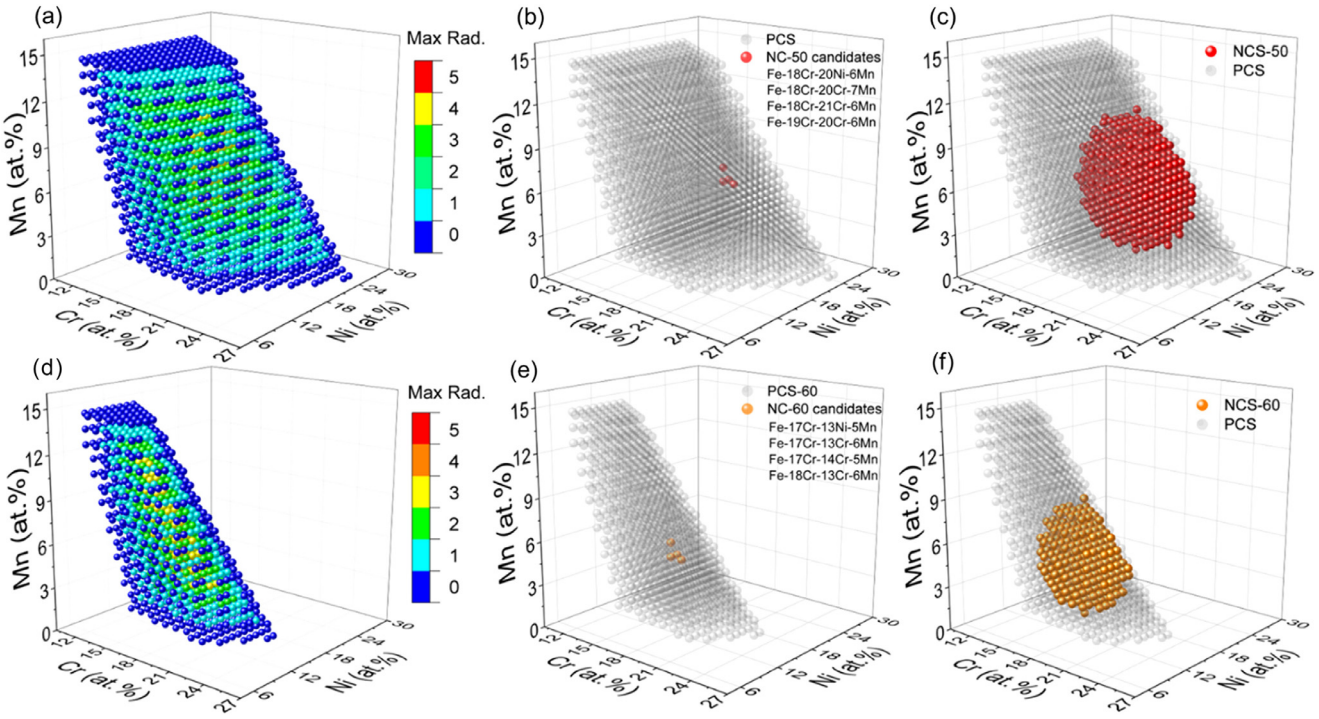

Fig. 4. Search for the nominal composition space. The maximum radius for each candidate composition within the PCS when the minimum Fe content is (a) 50 at.% and (d) 60 at.%. (b, e) The compositions with the highest maximum radius. (c, f) The constructed NCS considering different Fe limits.

2.3. Nominal composition space with maximum compositional flexibility

After acquiring the PCS and its associated mechanical properties, the nominal composition space (NCS) for potential CF-ASS can be determined. The goal of defining the NCS is to further refine the property range and provide guidance for the industrial production of CF-ASS.

In the first approximation, the NCS is conceptualized as a sphere (the composition variation is symmetrical for each element), wherein candidate compositions within the sphere should have a YS spread of ±20 MPa. The 20 MPa variation is chosen as it is roughly 10 % of the average YS predicted in Fig. 3(a) and further changes to this threshold can be imposed as needed in the future. The SFE is not used as a key restricting factor due to the predicted high SFE values for most alloys according to Fig. 3(b). Furthermore, the NCS must be a subset of the PCS to satisfy phase stability and corrosion resistance criteria. These conditions enable the construction of Fig. 4(a), which illustrates the maximum radius of the composition sphere with each candidate composition within the PCS considered as the centre. A simplified method was adopted to determine the maximum radius. For each candidate composition, the iterative search process considers six directions (i.e., ±Cr, ±Ni, and ±Mn).

During each iteration, the radius is incremented by 1 at.%; if any composition in any of the six directions exceeds the PCS, the increment is considered invalid, the last increment is recorded as the maximum radius for the candidate composition. If all compositions in the six directions fall within the PCS, the predicted YS values of these compositions are compared with that of the candidate composition. If any of the six predicted YS values exceed the ±20 MPa limit, the increment is deemed invalid.

As shown in Fig. 4(a), candidate compositions at the boundaries of the PCS have a maximum radius of 0, indicating that any deviation from the candidate composition would exceed the PCS. The maximum radius increases as candidate compositions move fur-

ther into the PCS. Four compositions with a maximum radius of 5 at.% are identified in the high Cr and Ni region (~20 at.% for both elements, Fig. 4(b)). Selecting one of the four compositions (Fe-18Cr-20Ni-6Mn, at.%) as the nominal composition (NC) and using a maximum radius of 5 at.%, the NCS is established, as shown in Fig. 4(c). This refined NCS contains 491 candidate compositions. Notably, this NCS does not precisely form a sphere, as some compositions within the sphere having a 5 at.% radius towards all directions may be outside of the original PCS. Furthermore, the SFE values of compositions within the NCS are all above 25 mJ/m^2 (Fig. S1 in Supplementary Information), implying that the deformation induced martensite should be absent upon deformation.

While the NCS in Fig. 4(c) presents a guideline for the production of CF-ASS, the compositions within this NCS feature high Cr and Ni contents, which are cost-intensive. Therefore, in a subsequent refinement, the minimum Fe content is raised to 60 at.% and the searching process is conducted again. The evolution of the maximum radius shown in Fig. 4(d) follows a similar trend as Fig. 4(a), albeit with the highest maximum radius reduced to 4 at.%. The candidate compositions now fall within the range of ~17 at.% Cr and 14 at.% Ni (Fig. 4(e)), closer to the common stainless steel alloying range. Using the Fe-17Cr-14Ni-5Mn (at.%) alloy as the nominal composition, the NCS depicted in Fig. 4(f) contains 238 compositions, considering the new Fe limit. In this case, the minimum SFE value within this NCS decreases to 25 mJ/m^2, which is still higher than the commonly acknowledged 20 mJ/m^2 threshold for deformation induced martensitic transformation. Thus, a change in magnetic properties should, in principle, be absent. In the following validation sections, the NC and NCS will be referenced based on their Fe limits. The NCS shown in Fig. 4(f) will be denoted as NCS-60 and the NCS shown in Fig. 4(c) will be referenced as NCS-50 in the validation section for brevity.

3. Experimental validation

In this study, 34 alloy compositions were selected for smelting and experimental investigation. The experiments aimed not only to assess the accuracy of the screening criteria and predictive models but also to demonstrate the stable property output of alloys within NCS-50 and NCS-60. Out of the 34 experimental alloys, 23 alloys are entirely within the PCS, while the remaining 11 alloys do not meet all screening criteria such as the presence of unwanted phases, lack of Cr or high alloying contents. These 11 alloys were made to validate the phase stability criteria. Fig. 5 shows the distribution of the smelted alloys mapped onto the normalized Cr-Ni-Mn ternary space. As shown in Fig. 5(a), the selected alloys are dispersed within the PCS, enabling the collection of representative validation data. Alloys outside the PCS due to low Fe content, high M_s temperature and low FCC content are shown in Fig. 5(b). It is worth noting that although the 11 alloys fall outside the 3-D composition space, some may reside in the normalized 2-D dimensional space due to composition normalization.

3.1. Experimental methods

Ingots weighing about 80 g were made by argon arc melting, and the purity of the source alloying elements are above 99.9 %. To ensure chemical uniformity, the ingots underwent at least 5 remelting cycles with magnetically stirring. The composition of each alloy was confirmed using optical emission spectroscopy (OES). Subsequently, the ingots were homogenized at 1200 °C in an argon atmosphere for 5 h, followed by water quenching. Plates with a thickness of 5 mm were extracted from the middle of the homogenized samples and cold rolled to a thickness of 2 mm (approximately 60 % thickness reduction). Finally, the cold-rolled sheets were annealed at 1200 °C for 2 h, and then water quenched to obtain a solid-solution treated sample.

X-ray diffraction (XRD) measurement was used to identify the phases present in different alloys. A Rigaku SmartLab 9 kW diffractometer (Cu source) was used, and the XRD scans were conducted between 2θ angles between 40° and 100° with a scan speed of 6°/min. Microstructural characterization of samples before and after deformation was performed using a field emission scanning electron microscope (FEG-SEM; ZEISS, Gemini 300) equipped with an electron backscatter diffraction (EBSD) detector (Oxford Instruments, Symmetry S2). The microscope was operated at an accelerating voltage of 20 kV, and EBSD scans were taken with a step size of 1.1 μm. The obtained EBSD maps were post-processed with the AZtecCrystal software. Both XRD and EBSD specimens were electropolished in a solution with a ratio of perchloric acid to alcohol ratio of 1:7.

Uniaxial tensile tests were conducted using a Shimadzu AGS-X tensile testing machine equipped with a 10 kN load cell and a video extensometer at a nominal strain rate of 10^{-3} s^{-1}. Dog-bone tensile specimens were cut along the cold rolling direction, with dimensions of 15 mm (gauge length), 4 mm (width), and 1.5 mm (thickness). At least two sets of tensile tests were performed on each composition to ensure the reliability of the data. Vickers hardness tests were performed using the HWDV-7S Vickers hardness tester with a 300 g load was applied for 10 s. Each alloy was subjected to at least 30 indentations. Before the tensile and hardness tests, the specimen surface was polished with 1500 grit SiC paper.

Electrochemical measurements were performed in the form of open circuit potential and potentiodynamic polarization tests using a VersaSTAT 3F electrochemical workstation. Potentiodynamic polarizaiton tests were performed in a 3.5 wt.% NaCl solution

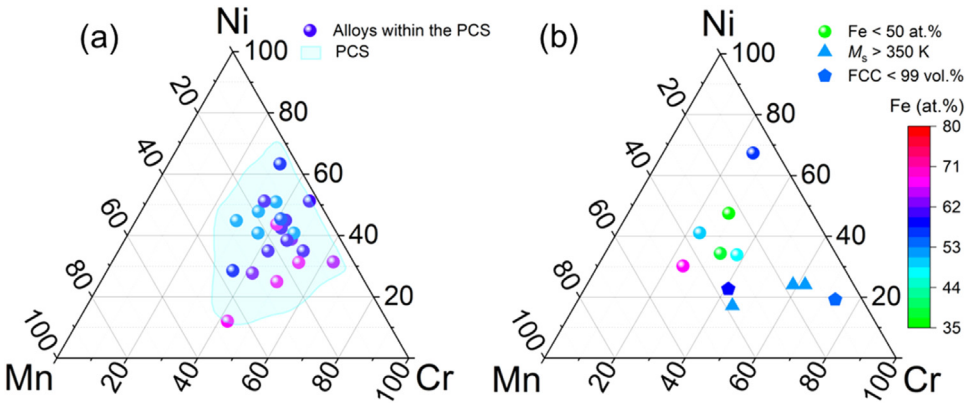

Fig. 5. The spatial distribution of experimental alloys mapped onto the Cr-Ni-Mn ternary space in atomic percentage. (a) Alloys within the PCS. (b) Alloys outside the PCS.

(open air, pH ~6) with a saturated calomel electrode (SCE) as the reference electrode and a Pt net as the counter electrode. The tests were conducted with a scan range of −0.3 V to +1.8 V with respect to the open circuit potential, which was obtained after stabilizing the sample for approximately 1 h. The scan rate for the tests was set at 0.5 mV/s.

3.2. Experimental results

3.2.1. Validation of screening criteria and property predictors

The XRD results of some of the smelted alloys are shown in Fig. 6 (XRD for all alloys in Fig. S2). Fig. 6(a, b) shows the phase analysis of the alloys within the PCS. Most samples exhibit a fully FCC microstructure, confirming the accuracy of the two screening criteria for phase stability. In Fig. 6(b), two alloys display the presence of a small amount of body centred cubic (BCC) or HCP phase, likely due to the high alloying addition of Cr/Mn, which leads to local chemical heterogeneity and resultant phase instability. The alloys in Fig. 6(c) lie outside the PCS due to Cr content <13 at.% or the Fe content <50 at.%. All XRD scans in Fig. 6(c) show full FCC characteristics, suggesting the potential extension of PCS, particularly for high Ni variants. Alloys in Fig. 6(d) fall outside the PCS as they fail to meet the phase stability criteria, with all showing mixed phases containing BCC and/or HCP phases. Notably, compositions such as Fe-19Cr-5Ni-2Mn (at.%, same for following compositions) and Fe-9Cr-5Ni-8Mn exhibit FCC contents <99 vol.% during austenization, while the rest have M_s greater than 350 K. These compositions with low phase stabilities are well predicted by the designed criteria. A comprehensive comparison between theoretical predictions and experimental results can be found in Table S3.

18 out of 21 alloys with fully FCC structures are selected for further testing in order to validate the accuracy of the performance prediction models. Tensile curves for the 18 alloys are available in Fig. S3. Fig. 7(a) presents a comparison between the experimental and predicted strengths. It can be seen that for all alloys with fully FCC microstructures, there is a good agreement between the predicted and experimental values, thus validating the strength prediction model used in this study. Although Fig. 7(b) shows that the yield strength of the experimental alloys is slightly lower compared to the commercial alloys, grain refinement, and cold working can be utilized to further adjust the properties during application.

The SFE of alloys within the PCS was previously calculated. To validate the accuracy of the calculations, the microstructure after deformation was examined. XRD results were not used to calculate the exact SFE values, as common methods rely on the deconvolution of the full-width at half maximum (FWHM) of the XRD peaks [44], which can be complicated by artifacts such as dislocation density and residual stresses. Moreover, the current work concerns more about the deformation modes and transformation products than the exact SFE values. Fig. 8 shows the EBSD results of 4 alloys after fracture, and the EBSD scans were taken near the fracture surface. The calculated SFE values for the alloys shown in Fig. 8(a–d) are 79, 51, 44, and 25 mJ/m^2, respectively. According to the common belief in the literature, only the last alloy should display significant deformation twinning and deformation induced martensite (DIM) should not appear in all samples. This is not the case as shown in Fig. 8. Specifically, the Fe-18Cr-25Ni-6Mn alloy, with an SFE well above 40 mJ/m^2, predominantly exhibits dislocation slip, evident from the presence of a high density of low-angle grain boundaries (LAGB) in Fig. 8(e). Meanwhile, the deformation mechanism of the Fe-21Cr-14Ni-5Mn and Fe-17Cr-14Ni-9Mn, with SFE closer to 40 mJ/m^2, is primarily governed by deformation twinning, evidenced by twin boundary (TB) contents of 61.2 % and 57.4 %, respectively (Fig. 8(f, g)). The Fe-16Cr-8Ni-8Mn

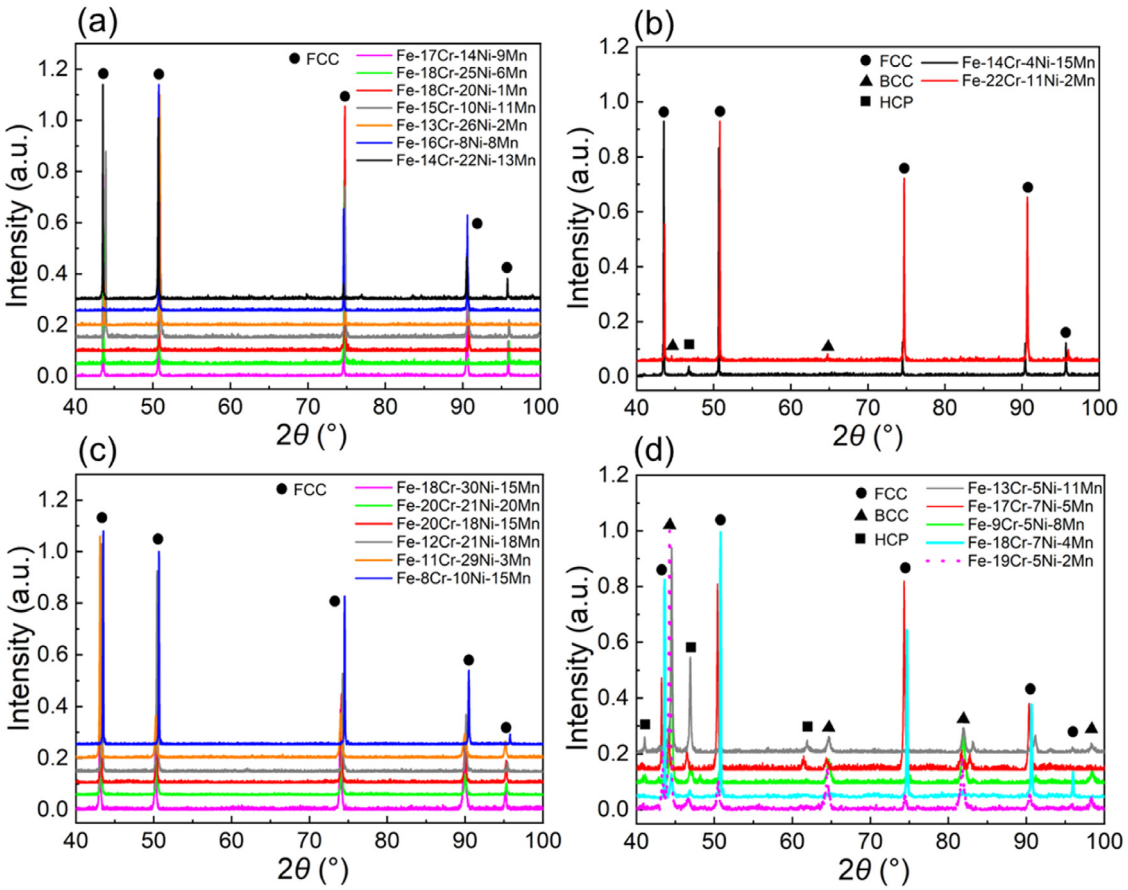

Fig. 6. XRD patterns of the smelted alloys. (a, b) Alloys within the PCS. (c, d) Alloys outside the PCS due to (c) composition and (d) phase stability issues.

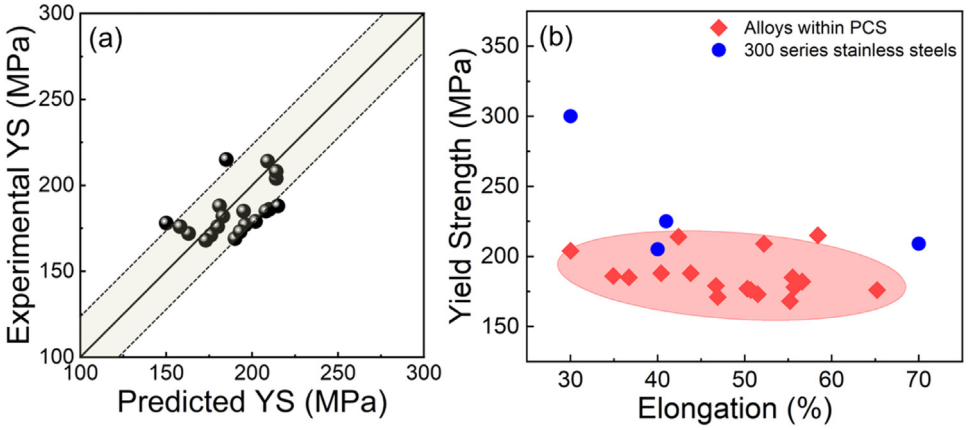

Fig. 7. (a) The comparison between the predicted yield strength and the experimental yield strength for 18 alloys within the PCS and fully FCC microstructures. (b) Elongation and yield strength of experimental alloys and standard 300 series stainless steels [42,43].

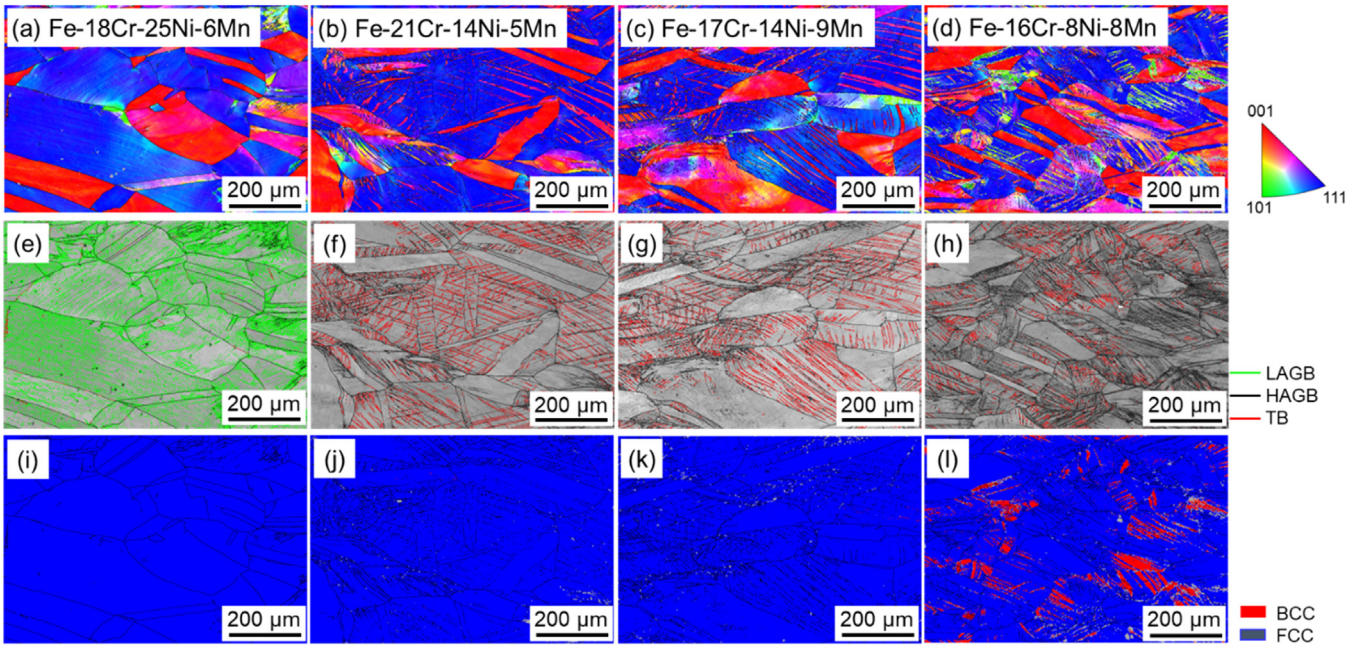

Fig. 8. (a–d) EBSD IPF, (e–h) band contrast and (i–l) phase maps of four alloys after deformation. The coloured lines in (e–h) represent the low angle grain boundaries (LAGB in green, $\theta \leq 2°$), high angle grain boundaries (HAGB in black, $2° < \theta \leq 15°$), and twin boundaries (TB in red).

alloy, with the lowest SFE of 25 mJ/m^2, exhibits a significantly reduced TB content of 34.5 % (Fig. 8(h)), along with the emergence of α'-martensite (7.6 % from EBSD, Fig. 8(l)), which should typically be observed in alloys with SFE lower than 20 mJ/m^2[44]. Although the current calculation method seems to overestimate SFE, the observed trend in the evolution of deformation mechanisms remains consistent (i.e., lower SFE results in a transition from dislocation slip to TWIP and TRIP). Since most of the alloys within both NCS-50 and NCS-60 have SFE above 25 mJ/m^2 (Fig. S1), the deformation modes for most of those alloys should be dislocation slip and TWIP, and does not involve the formation of ferromagnetic α'-martensite, satisfying the criteria of the current design.

Fig. 9 shows the pitting potentials of the alloys within the PCS and the comparison with common 200 and 300 series stainless steels. The dashed black line in Fig. 9 represents the pitting potential of a commercial 316 stainless steel under the same test conditions as the experimental alloys. Detailed polarization curves can be found in Fig. S4. Data for 200 and 300 series stainless steels are obtained from the work of Truman et al. with testing conditions similar to those used in the current work [45–47]. The pitting potentials of the designed alloys are mainly distributed between 0 and 300 mV (SCE), well within the range observed for 200 and 300 series stainless steels, ensuring the basic corrosion resistance of the CF-ASS. Notably, while the alloying content for Cr, Ni, and Mn varies significantly in the current dataset, the influence of these elements on the pitting potential is not readily apparent. Similar trends can also be observed in the literature data that the pitting potential does not correlate directly with the variation of a single element but rather scatters throughout the examined compositions [48]. This could be attributed to the large variation of alloying elements used in the current study and the detailed correlation between pitting potentials and interacting alloying additions requires further studies. Nevertheless, these results suggest the possibility to achieve comparable pitting potentials within a broad composition space.

3.2.2. Property variation for compositionally flexible alloys

From the established NCS-50 and NCS-60, two nominal compositions, Fe-18Cr-20Ni-6Mn and Fe-17Cr-14Ni-5Mn, were selected

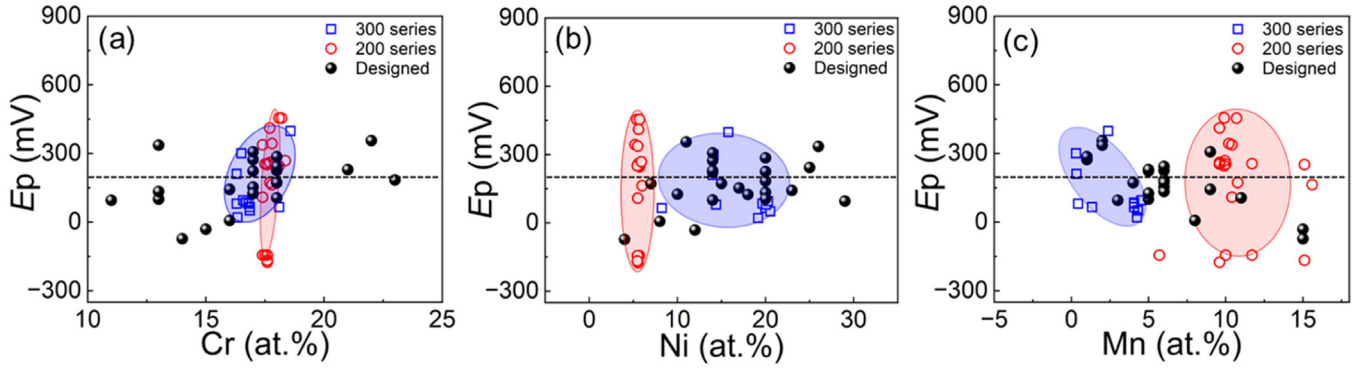

Fig. 9. Corrosion performance of the smelted alloys within the PCS compared to common austenitic steels [45–47,49–51]. (a), (b) and (c) show the corresponding pitting potentials of the alloys with different Cr, Ni, Mn contents, respectively.

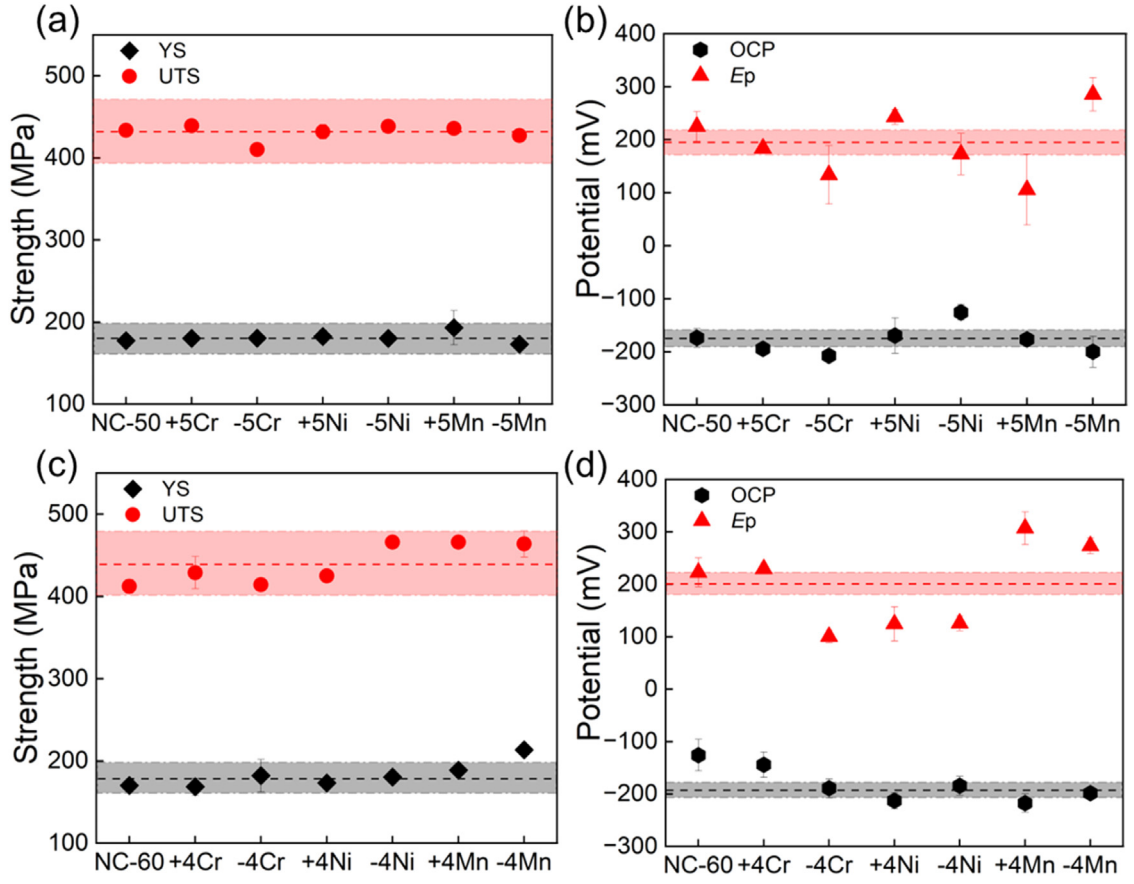

Fig. 10. Tensile and corrosion properties of alloys from NCS-50 and NCS-60. (a, b) Properties for NC-50 and its 6 variants with ±5 at.% changes in each alloying element. (c, d) Properties for NC-60 and its 6 variants with ±4 at.% changes in each alloying element. The dashed lines represent the average values of the seven alloys and the shaded regions represent 10 % variation with respect to the means.

as the nominal compositions and designated as NC-50 and NC-60, respectively. These compositions, along with their variant alloys extending to the maximum radius in six directions, were chosen to assess the stability of mechanical and corrosion performance. NC-50 has a maximum radius of 5 at.%, while NC-60 has a maximum radius of 4 at.%. The tensile and corrosion properties of NC-50 and its variant alloys in six directions are shown in Fig. 10(a, b). The yield strength centres around 180 MPa, and the tensile strength is concentrated at about 440 MPa. Open circuit potential hovers around −150 mV (SCE), while the pitting potential fluctuates around 200 mV (SCE). The shaded regions represent 10 % variation from the mean for each property. It is observed that the properties generally fall within the shaded region, except for the pitting potential. For NC-60 and its variants, which closely resemble NC-50 in composition except for significant reduction in Ni content, the average property values closely mirror those of NC-50 (Fig. 10(c, d)). The only difference is that the scatter in the pitting potential often exceeds the 10 % range, leading to variations around 100 mV. These results suggested that relatively consistent mechanical and corrosion performance can be achieved across compositions within both NCS. Furthermore, the observed mechanical and corrosion property ranges are comparable to the basic properties of 200 and 300 series stainless steels available in the market, further validating the CF-ASS concept.

4. Discussion

The experimental results shown in the previous section demonstrate that the phase stability criteria and performance predictors outlined in Section 2 are generally applicable to the PCS obtained, albeit with the SFE showing the largest discrepancy. Further validation of the two nominal compositions and composition within the NCS indicates the potential to achieve relatively stable properties with varying compositions in the NCS. Among the four key properties shown in Fig. 10, only the pitting potential varies significantly with different alloying elements, resulting variations of ±100 mV. The following sections will first discuss the practical implementation of the CF-ASS concept and then address the limitations of current calculation methods and what may be done in the future.

4.1. Roadmap to CF-ASS using co-mingled stainless steel scraps

Fig. 10 shows initial evidence suggesting that both mechanical and corrosion performances can remain relatively stable within NCS-50 and NCS-60. This section discusses the feasibility of producing these alloys using existing stainless steel scraps. Fig. 11(a, d) shows the positioning of NCS-50 and NCS-60 in the Cr-Ni-Mn composition space, along with common 200 and 300 series stainless steel grades as comparison. Due to the higher Ni content of the NCS-50, it shows no overlap with existing 300 series grades. This situation changes for NCS-60, as its top-left corner coincides with some existing 300 series grades. These comparisons reveal that while some portions of the NCS have been explored previously, much of it remains uncharted territory in the commercial market. The main reason for the absence of such products is that the NCS proposed here require both Ni and Mn alloying elements, departing from the development goals of 200 and 300 series stainless steels. The inclusion of both austenite stabilizers is considered redundant and economically unfeasible. However, if the demand for 200 series stainless steels (or the Fe-Cr-Ni-Mn series in general) continues to rise, the blending of 200 and 300 series stainless steel scraps will be inevitable in the future. Exploring the NCS space proposed here will provide guideline for the recycling of such co-mingled scrap sources. Fig. 11(b–d, f) demonstrates how mixed 205/304 and 201/316 scraps can be used to create compositions within NCS-50 and NCS-60 by incorporating ferronickel with varying nickel contents. Alloys in NCS-50 can be obtained by blending 304, 205, and FeNi70 (70 wt.% nickel and 30 wt.% iron) in mass ratios of 58 %, 19 %, and 23 %, as exemplified by the blue dots in Fig. 12(b). The blending strategy is closely related to NCS compositions and the grade of ferronickel. Since NCS-50 has a higher overall nickel content, achieving NCS-50 with a blend of 200 and 300 series scraps (Fig. 11(b, c)) requires a minimum of 50 wt.% nickel in the ferronickel (i.e., FeNi50). However, the area corresponding to FeNi50 in the ternary diagram indicates that only a small amount of the alloy in NCS-50 can be obtained by blending. As the Ni content in ferronickel increases, more compositions in NCS-50 can be obtained through co-mingling, along with a broader range of 300 and 200 scraps being added (Fig. 11(c)). For example, with the addition of 20 wt.% FeNi70, 304, and 205 scraps can be added in the ranges of 30 wt.%–80 wt.% and 0–50 wt.%, respectively. Meanwhile, the additive range of the offcuts is also limited by the composition of the scraps. When adding 205 scraps with lower Ni content to obtain NCS-50 and NCS-60, the addition of 205 scraps is limited to <50 wt.% for both. In this case, it is necessary to add a higher grade of ferronickel or to blend with scraps with higher Ni content to increase the proportion of 205 scraps added. Due to the constraint on the Cr content, the addition of 200 and 300 scraps is inversely proportional to each other. Moreover, it can be

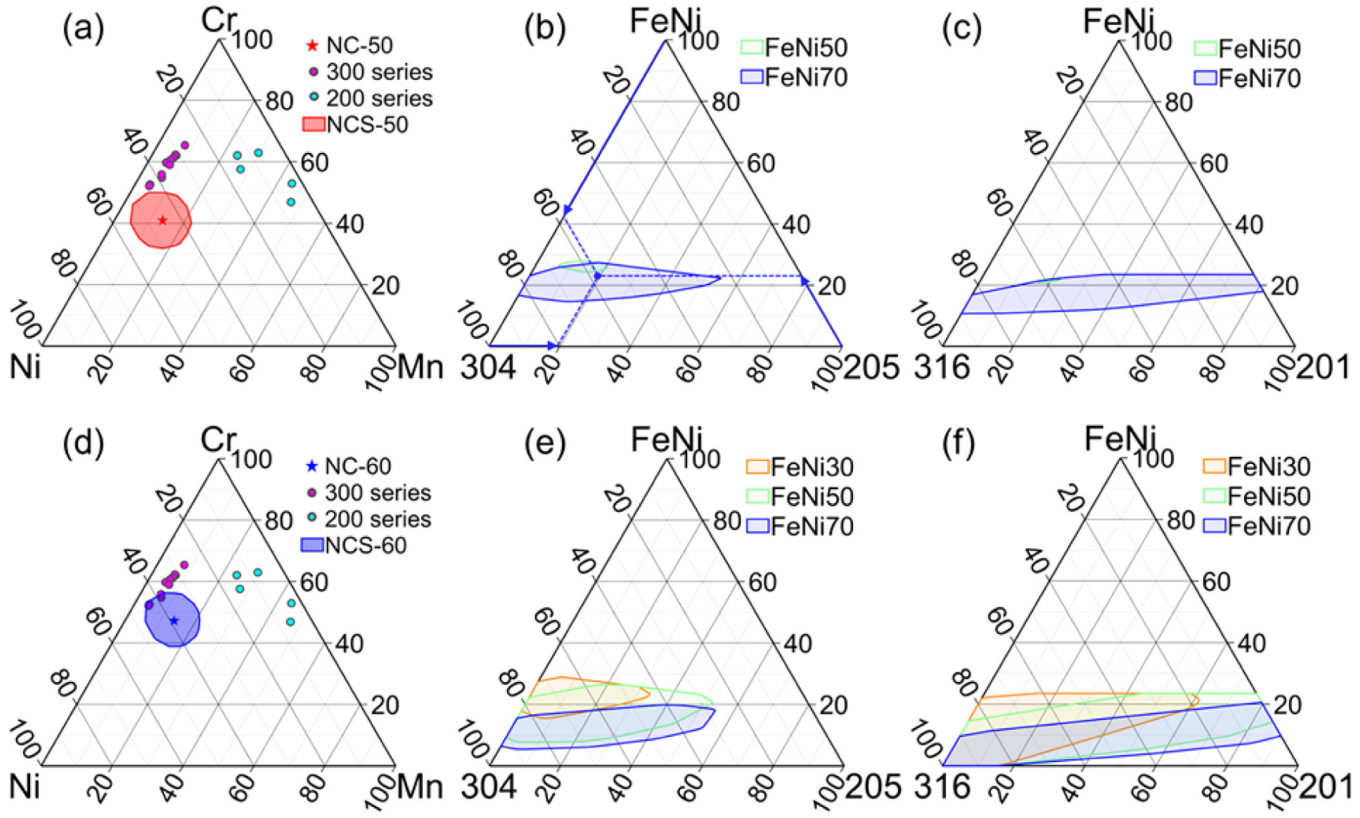

Fig. 11. Towards mixed scrap recycling in austenitic stainless steels. (a, d) The comparison between the two NCS and common stainless steel grades, unit: at.%. (b, e) Mixing strategy to achieve compositions within the two NCS using mixed 304 and 205 scraps with FeNi sources of different Ni contents, unit: wt.%. (c, f) Mixing strategy to achieve compositions within the two NCS using mixed 316 and 201 scraps with FeNi sources of different Ni contents, unit: wt.%.

seen that the amount of added ferronickel, even for FeNi70, is not higher than 30 wt.%, implying the amount of additional new material will still be low, signifying the advantage of scrap mixing. Similar trends are observed for NCS-60 (Fig. 11(e, f)). The reduced nickel requirement in NCS-60 permits the use of ferronickel with lower nickel content (FeNi30), and the minimum permissible additions are reduced. As shown in Fig. 12(f), when 300 series scraps are sufficient, it is not necessary to add additional ferronickel. Only a large amount of 316 scraps and a small amount of 201 scraps are required, with additions ranging from 80 wt.% to 100 wt.% and 0 to 20 wt.%, respectively. In principle, these pseudo-tertiary diagrams can be generated for any given mix of 200 and 300 series or various combinations of different scrap sources. Therefore, the proposed NCS and the representation shown in Fig. 12 provide guidance for future recycling co-mingled stainless steel scraps.

Fig. 11 has shown that ferronickel with a high Ni content is required when NCS is made using mixed 200 and 300 series stainless steels. Moreover, the high demand for Ni and Mn in NCS is contrary to the design concept of conventional stainless steel, which may increase the alloying cost and hinder the adaptation of such recycling method. However, when high Ni and Mn alloyed variants such as NC-50 and NC-60 are further recycled, less Ni addition will be required. Fig. 12 shows the mixing strategy for NC, 316/201 stainless steels, and different grades of ferronickel. Compared to Fig. 11, when NC enters the cycle, the grade of ferronickel required is greatly reduced (i.e., down to FeNi8) and the minimum percentage of ferronickel allowed to be added also decreases. In the lower left corner of the figures, it is even possible to get back to NCS without the addition of new ferronickel, which greatly reduces the cost and promotes circular recycling. Meanwhile, the area in which NC and 300/200 scraps are allowed to be added has been further enlarged, reducing the limitation on mixing ratio and making the blending more efficient. It is worth noting that when NC enters the circulation, all of the mixing paths shown in Fig. 12 expand outward from the lower right corner. Compared to Fig. 11, the mixing paths shown in Fig. 12 still exhibit a large area of overlap while both ferronickel grades and stainless steel scraps are changing, reducing the constraints on the co-mingled gold species and mixing ratios. Ideally, as more and more alloys close to the NCS enter the cycle, there will be less need for new ferronickel, and any of the alloys from NCS can be put together by recycling scraps and direct remelting. Lastly, it is observed that although NCS-50 provides greater compositional flexibility, NCS-60 demonstrates a broader range of blending pathways when obtained through the recycling of widely used conventional stainless steel scraps. This indicates that the alloy design of NCS-60 is more aligned with economic viability and sustainability.

4.2. Limitations of the current calculation methods

In this study, M_s serves as a criterion to ensure the phase stability of the alloy at room temperature, and its calculation accuracy directly affects the reliability of the PCS. While the XRD results indicate that most of the smelted alloys do not exhibit martensitic transformation, the exact M_s values may not agree well with the predicted values. Fig. 13(a) shows the experimental results of two alloys with different M_s values: one with a predicted M_s below the 350 K threshold (Fe-18Cr-6Ni-10Mn, 330 K) and the other predicted to have an M_s higher than 350 K (Fe-9Cr-5Ni-8Mn, 425 K). The experimental results reveal that the M_s temperature of Fe-18Cr-6Ni-10Mn is below room temperature, and the M_s temperature of Fe-9Cr-5Ni-8Mn is 365 K. Both predicted results are higher than observed. Reviewing the database used to train the DDM-CNN model, two main reasons for the high prediction results of

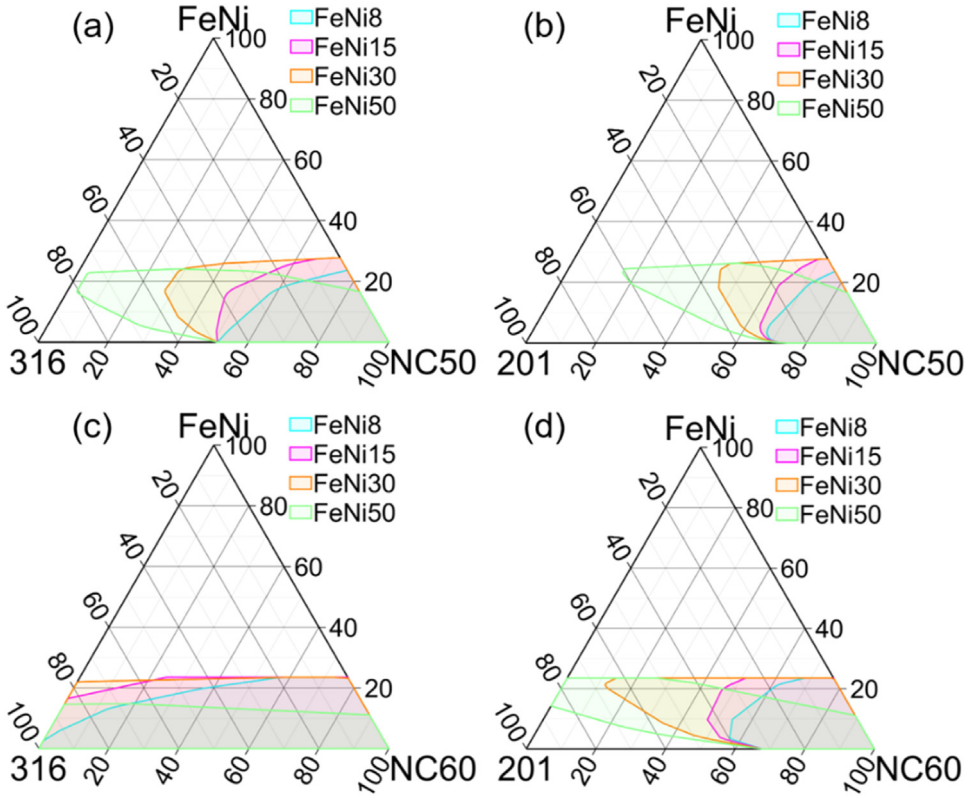

Fig. 12. The effect of mixing NC with existing commercial stainless steels. (a, b) Mixing strategy to achieve compositions within the NCS-50 using mixed 316/201 and NC-50 scraps with FeNi sources of different Ni contents, unit: wt.%. (c, d) Mixing strategy to achieve compositions within the NCS-60 using mixed 316/201 and NC-60 scraps with FeNi sources of different Ni contents, unit: wt.%.

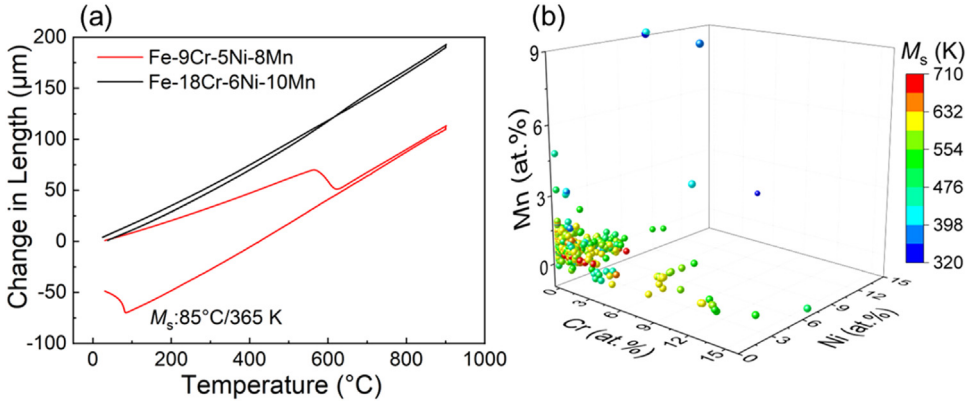

Fig. 13. (a) Dialotometry curves of two candidate alloys with predicted M_s values around the phase stability criterion. (b) Alloys used to construct the DDM-CNN model and their corresponding M_s values.

the M_s values are identified. Firstly, the original database primarily focused on carbon steels, where carbon significantly influences the M_s value. Since the alloys in this study lack significant carbon additions, the model's ability to extrapolate to ultra-low carbon regimes may be affected. Secondly, although the DDM-CNN model demonstrates good extension to steels with high alloying contents including Cr, Ni, and Mn, the majority of data entries cluster at the low alloying content corner, with few from high alloying steels (Fig. 13(b)). Consequently, the model was constructed with limited data from high alloying compositions, resulting in prediction uncertainties when the variation of multiple alloying elements exceed the clustered regions of the original database. This is also the reason that the M_s criterion was set to 350 K and not room temperature as the uncertainty may be greater than 50 K as demonstrated in Fig. 13(a). Further experimental and machine learning work on the exploration of the entire Fe-Cr-Ni-Mn composition space is needed in the future.

Apart from the martensite start temperature, the calculation for the SFE values also presents challenges. While the transition from deformation slip to deformation-induced martensitic transformation correlates with decreasing SFE values, there appears to be an overestimation of the exact SFE values when compared to the common range associated with each deformation mode. This discrepancy led to the decision not to impose the SFE value as a constraining factor in constructing the nominal composition space. In the current approach, determining the interfacial energy and molar free energy associated with the $\gamma \rightarrow \varepsilon$ transformation relies on thermodynamic data extracted from the literature. However, these data primarily consider pure elemental contributions and binary interactions, failing to account for the complex interactions within the current quaternary system. In addition, the reliance on extrapolated and scattered experimental data for thermodynamic information introduces potential unreliability, particularly in complex systems. Dedicated thermodynamic studies are required to address this issue. Alternatively, changing the estimation of SFE values to direct prediction of the deformation mode using machine learning approaches based on alloying chemistries could offer a solution. Moreover, constructing a large experimental dataset including full stress-strain curves for high-alloying austenitic stainless steel systems would enable the development of models to predict complete tensile behaviours directly, facilitating the sequential construction of associated processing windows.

5. Conclusions

The present work proposes austenitic stainless steels with flexible compositions (CF-ASS), offering insights into the future recycling of large quantities of 200 and 300 series stainless steel scrap, particularly when scrap mixing becomes unavoidable. The following conclusions can be drawn from the current work:

(1) A preliminary composition space (PCS) consisting of 2898 alloys was obtained following phase stability, corrosion resistance, and source availability screening. The predicted yield strength within the PCS ranges from 130 MPa to 230 MPa, and most alloys have SFE higher than 36 mJ/m^2.
(2) Based on the PCS, two nominal compositional spaces (NCS) were identified to deliver alloys with flexible compositions but stable property outcomes. The NCS-50 permits compositional variation within a 5 at.% radius while maintaining mechanical properties of 180 MPa in yield strength and 440 MPa in tensile strength. The open-circuit potential and pitting potential for these alloys are around −150 mV and 200 mV (SCE), respectively. These properties are comparable to common stainless steels in the market. Adjusting the minimum Fe content to 60 at.% offers a means to reduce alloying costs, but at the expense of compositional flexibility (to a 4 at.% radius).
(3) It was demonstrated that both NCS can be achieved by mixing 200 and 300 series stainless steel scraps with the addition of ferronickel. The required grade and quantity of ferronickel depends on the Ni range of the NCS. With sufficient 300 series scraps, the need for additional ferronickel decreases. This blending strategy can become more flexible when stainless steels having the NC proposed in this work enter the recycling scheme, further reducing the amount of additional nickel.

Declaration of generative AI and AI-assisted technologies in the writing process

During the preparation of this work, the author(s) used ChatGPT 3.5 in order to improve readability and language. After using this tool/service, the author(s) reviewed and edited the content as needed and take(s) full responsibility for the content of the publication.

Declaration of competing interest

The authors declare that they have no known competing financial interests or personal relationships that could have appeared to influence the work reported in this paper.

CRediT authorship contribution statement

Qiqi Liu: Writing – review & editing, Writing – original draft, Methodology, Investigation, Conceptualization. **Lingyu Wang:**

Writing – review & editing, Writing – original draft, Investigation, Conceptualization. **Chenchong Wang:** Writing – review & editing, Software. **Yuxiang Wu:** Writing – review & editing. **Zhen Zhang:** Software, Methodology. **Xiaolu Wei:** Software, Methodology. **Yong Li:** Software, Methodology. **Jiahua Yuan:** Methodology. **Jun Hu:** Writing – review & editing. **Dengping Ji:** Resources. **Sybrand van der Zwaag:** Writing – review & editing. **Yizhuang Li:** Writing – review & editing. **Wei Xu:** Writing – review & editing, Supervision, Project administration, Funding acquisition.

Acknowledgments

This work was financially supported by the National Key Research and Development Program (No. 2023YFB3712403) and the National Natural Science Foundation of China (Nos. 52201112, 52071066, U22A20106, and U22A20173). The authors appreciate the fruitful discussion with Prof. Chris Hutchinson.

Supplementary materials

Supplementary material associated with this article can be found, in the online version, at doi:10.1016/j.jmst.2024.11.041.

References

[1] T. Lei, D. Wang, X. Yu, S. Ma, W. Zhao, C. Cui, J. Meng, S. Tao, D. Guan, Nature 622 (2023) 514–520.
[2] P. Wang, M. Ryberg, Y. Yang, K. Feng, S. Kara, M. Hauschild, W.-Q. Chen, Nat. Commun. 12 (2021) 2066.
[3] Q. Zhang, W. Chen, W. Ling, Int. J. Hydrog. Energy 47 (2022) 41183–41194.
[4] Y. Zhang, Q. Yue, X. Chai, Q. Wang, Y. Lu, W. Ji, J. Clean. Prod. 361 (2022) 132289.
[5] M.B. Ledari, H. Khajehpour, H. Akbarnavasi, S. Edalati, Int. J. Hydrog. Energy 48 (2023) 36623–36649.
[6] D. Patnaik, A.K. Pattanaik, D.K. Bagal, A. Rath, Int. J. Hydrog. Energy 48 (2023) 23449–23458.
[7] D. Raabe, M. Jovičević-Klug, D. Ponge, A. Gramlich, A.K. da Silva, A.N. Grundy, H. Springer, I.S. Filho, Y. Ma, Annu. Rev. Mater. Sci. 54 (2024) 247–297.
[8] H. Ohno, K. Matsubae, K. Nakajima, S. Nakamura, T. Nagasaka, J. Ind. Ecol. 18 (2014) 242–253.
[9] H. Ohno, K. Matsubae, K. Nakajima, Y. Kondo, S. Nakamura, T. Nagasaka, Resour. Conserv. Recycl. 100 (2015) 11–20.
[10] B.K. Reck, T.E. Graedel, Science 337 (2012) 690–695.
[11] L. Brooks, G. Gaustad, A. Gesing, T. Mortvedt, F. Freire, Waste Manage. 85 (2019) 519–528.
[12] X. Li, K. Lu, Nat. Commun. 16 (2017) 700–701.
[13] X. Li, K. Lu, Science 364 (2019) 733–734.
[14] Q. Lu, Q. Lai, Z. Chai, X. Wei, X. Xiong, H. Yi, M. Huang, W. Xu, J. Wang, Sci. Adv. 7 (2021) 1–8.
[15] H. Zhan, G. Zeng, Q. Wang, C. Wang, P. Wang, Z. Wang, Y. Xu, D. Hess, P. Crepeau, J. Wang, J. Mater. Sci. Technol. 154 (2023) 251–268.
[16] S. Samberger, I. Weißensteiner, L. Stemper, C. Kainz, P.J. Uggowitzer, S. Pogatscher, Acta Mater. 253 (2023) 118952.
[17] K.E. Daehn, A. Cabrera Serrenho, J.M. Allwood, Environ. Sci. Technol. 51 (2017) 6599–6606.
[18] X. Shen, D. Görzen, Z. Xu, B. Blinn, W. Bleck, T. Beck, U. Krupp, W. Song, Materialia 26 (2022) 101626.
[19] Z. Xu, X. Shen, T. Allam, W. Song, W. Bleck, J. Mater. Res. Technol. 17 (2022) 2601–2613.
[20] D. Raabe, D. Ponge, P.J. Uggowitzer, M. Roscher, M. Paolantonio, C. Liu, H. Antrekowitsch, E. Kozeschnik, D. Seidmann, B. Gault, F. De Geuser, A. Deschamps, C. Hutchinson, C. Liu, Z. Li, P. Prangnell, J. Robson, P. Shanthraj, S. Vakili, C. Sinclair, L. Bourgeois, S. Pogatscher, Prog. Mater. Sci. 128 (2022) 100947.
[21] M.R. Barnett, M. Senadeera, D. Fabijanic, K.F. Shamlaye, J. Joseph, S.R. Kada, S. Rana, S. Gupta, S. Venkatesh, Acta Mater. 200 (2020) 735–744.
[22] J.L. Cann, A. De Luca, D.C. Dunand, D. Dye, D.B. Miracle, H.S. Oh, E.A. Olivetti, T.M. Pollock, W.J. Poole, R. Yang, C.C. Tasan, Prog. Mater. Sci. 117 (2021) 100722.
[23] D.B. Miracle, O.N. Senkov, Acta Mater. 122 (2017) 448–511.
[24] I. Daigo, Y. Matsuno, Y. Adachi, Resour. Conserv. Recycl. 54 (2010) 851–863.
[25] X. Lu, H. Ohno, O. Takeda, T. Miki, Y. Sasaki, H. Zhu, T. Nagasaka, J. Ind. Ecol. 26 (2022) 1701–1713.
[26] S. Nakamura, Y. Kondo, K. Nakajima, H. Ohno, S. Pauliuk, Environ. Sci. Technol. 51 (2017) 9469–9476.
[27] K. Nakajima, H. Ohno, Y. Kondo, K. Matsubae, O. Takeda, T. Miki, S. Nakamura, T. Nagasaka, Environ. Sci. Technol. 47 (2013) 4653–4660.
[28] E.T. Kim, M. Ishtiaq, J. Chan Han, K.K. Ko, H.J. Bae, H. Sung, J.G. Kim, J.B. Seol, Scr. Mater. 203 (2021) 114112.
[29] R. Ke, X. Wan, Y. Zhang, C. Hu, K. Wu, Mater. Charact. 184 (2022) 111689.
[30] D. Sandoval, Is Nickel Dulling?, https://www.recyclingtoday.com/article/is-nickel-dulling-/, November 11, 2005.
[31] D. Raabe, C.C. Tasan, E.A. Olivetti, Nature 575 (2019) 64–74.
[32] J. Johnson, B.K. Reck, T. Wang, T.E. Graedel, Energy Policy 36 (2008) 181–192.
[33] Y. Ma, B. Xu, B. Yang, D. Liu, Vacuum 110 (2014) 136–139.
[34] C. Wang, K. Zhu, P. Hedström, Y. Li, W. Xu, J. Mater. Sci. Technol. 128 (2022) 31–43.
[35] K.H. Lo, C.H. Shek, J.K.L. Lai, Mater. Sci. Eng. R-Rep. 65 (2009) 39–104.
[36] K.N. Sasidhar, N.H. Siboni, J.R. Mianroodi, M. Rohwerder, J. Neugebauer, D. Raabe, npj Mater. Degrad. 6 (2022) 71.
[37] C. Varvenne, A. Luque, W.A. Curtin, Acta Mater. 118 (2016) 164–176.
[38] Z. Li, S. Ma, S. Zhao, W. Zhang, F. Peng, Q. Li, T. Yang, C.-Y. Wu, D. Wei, Y.-C. Chou, P.K. Liaw, Y. Gao, Z. Wu, Mater. Today 63 (2023) 108–119.
[39] H.B.V.G. Gavrilyuk, in: High Nitrogen Steels, first ed., Springer-Verlag, Berlin, 1999, pp. 135–201.
[40] S. Curtze, V.T. Kuokkala, A. Oikari, J. Talonen, H. Hänninen, Acta Mater. 59 (2011) 1068–1076.
[41] J.S. Aristeidakis, G.N. Haidemenopoulos, Acta Mater. 193 (2020) 291–310.
[42] C. Zheng, C. Liu, M. Ren, H. Jiang, L. Li, Mater. Sci. Eng. A 724 (2018) 260–268.
[43] M. Zhao, H. Wu, J. Lu, G. Sun, L. Du, Mater. Charact. 194 (2022) 112360.
[44] M. Walter, L. Mujica Roncery, S. Weber, L. Leich, W. Theisen, J. Mater. Sci. 55 (2020) 13424–13437.
[45] J.E. Truman, M.J. Coleman, K.R. Pirt, Br. Corros. J. 12 (1977) 236–238.
[46] N. Bui, A. Irhzo, F. Dabos, Y. Limouzin-Mare, Natl. Assoc. Corros. Eng. 39 (1983) 491–496.
[47] R. Bandy, D.V. Rooyen, Natl. Assoc. Corros. Eng. 39 (1983) 227–236.
[48] Y. Song, L. Yan, X. Pang, Y. Su, L. Qiao, K. Gao, Corros. Sci. 196 (2022) 110028.
[49] B.E. Wilde, E. William, Corrosion 117 (1970) 775–779.
[50] E. Lunarska, Z. Szklarska-Smialowska, M. Janik-Czachor, Corrosion 31 (1975) 231–234.
[51] M. Janik-Czachor, E. Lunarska, Z. Szklarska-Smialowska, Corrosion 31 (1975) 394–398.